A robust super-resolution approach with sparsity constraint in acoustic imaging

Ning Chu, José Picheral, Ali Mohammad-Djafari

A robust super-resolution approach via sparsity constraint in near-field wide-band aeroacoustic imaging ☆

Ning CHU[a,1,*], José PICHERAL[b,**], Ali MOHAMMAD-DJAFARI[a,**]

[a] *Laboratoire des signaux et systèmes (L2S), CNRS-SUPELEC-UNIV PARIS SUD, 91192 GIF-SUR-YVETTE, FRANCE*
[b] *SUPELEC, Département du Signal et Systèmes Electroniques, 91192 GIF-SUR-YVETTE, FRANCE*

Abstract

Aeroacoustic imaging is a standard technique for mapping locations and powers of aeroacoustic sources with microphone arrays. Recently the deconvolution-based methods, like DAMAS and its extensions, have greatly improved spatial resolution of conventional beamforming method and become a breakthrough in aeroacoustic imaging. But neither the DAMAS nor most of other classical methods are robust to background noise, nor do they provide a wide dynamic range of power estimation, particularly in the low Signal-to-Noise Ratio (SNR) situation.

In this paper, in order to improve the robustness, we first propose an improved forward model of aeroacoustic propagation by considering background noise and open wind tunnel effect. To obtain high spatial resolution in poor SNR cases, we then propose a robust super-resolution approach via sparsity constraint to reconstruct source powers and positions, and jointly estimate the variance of background noise. The robust sparsity constraint is adaptively estimated by the sparsity of source spatial distribution. Our approach is compared with some of the state-of-the-art methods on simulated, real data and hybrid data. The main advantages of the proposed approach are robustness to noise, a wide dynamic power range and super spatial resolution. It is feasible to apply it in near-field wide-band monopole and extended source imaging based on the 2D non-uniform microphone array in open wind tunnel tests.

Keywords: Near-field wide-band aeroacoustic imaging, robust super-resolution, sparsity constraint

1. Introduction

Aeroacoustic imaging refers to the localization and estimation of aeroacoustic sources, it can provide insight into aeroacoustic mechanisms and properties, which is usually used for designing quiet and comfortable vehicles, machinery and concert halls in civil domain, as well as the aeroacoustic surveillance and marine SONAR system in military applications [1–6]. Recently, near-field wide-band aeroacoustic imaging based on the Non-Uniform microphone Array (NUA) has been widely studied and applied in open wind tunnel tests. [7–9]. The advantage of NUA array is that with fewer antenna, it yields almost the same performance as the uniform array with larger number of sensors, which can lower computation burden as discussed in [10]. Classical methods of aeroacoustic imaging could be loosely classified as: Near-field Aeroacoustic Holography (NAH), Back Projection (BP) methods (Beamforming, Capon etc.), Subspace Separation methods (MUSIC

☆ Paper partly based on that accepted at the IEEE International Symposium on Signal Processing and Information Technology (ISSPIT2011) pp 286-289, Bilbao, Spain, Dec.14-17,2011.

* Principal corresponding author: Ning.CHU@lss.supelec.fr (Ning CHU). Tel. : +33 (0)1 69 85 1743. Fax : 00 33 (0)1 69 85 17 65

** Corresponding author:

Email addresses: jose.picheral@supelec.fr (José PICHERAL), djafari@lss.supelec.fr (Ali MOHAMMAD-DJAFARI)

[1] The author's PhD study is financed by China Scholarship Council (CSC) and École Supérieure d'Électricité (SUPELEC) FRANCE

etc.), deconvolution methods (CLEAN and DAMAS etc.) and inverse methods (SVD-ℓ_1 norm, Compressed Sensing, Bayesian inference approach etc). There is no one-fits-all methods, and all of them confront the challenges of how to achieve high spatial resolution, wide dynamic range and low computational burden at the same time. The Near-field Acoustic Hologram (NAH) [11, 12] provides good resolution which is equal to the antenna interval over the entire working frequency range, but it is restricted to use at high frequency due to the limitation of hologram size, and also it could not work well on the NUA array as commented in [1]. The beamforming method [2, 13] is direct, simple and fast, but its spatial resolution and dynamic range are limited due to its high sidelobes and spatial aliasing effects, especially at low frequency and on the NUA array. MUltiple SIgnal Classification (MUSIC) [14] greatly improves the beamforming resolution, but it requires high SNR and the exact number of sources, moreover MUSIC could not directly estimate source powers. Based on signal subspace separation, Orthogonal Beamforming (OB) [15] can work better than MUSIC, but OB still needs to know the source number beforehand. Near-Field Focalization (NFF) [16, 17] has high resolution at high frequencies, but it is better to use it in combination with the NAH or beamforming method. The CLEAN [18] and RELAX methods [19] are deconvolution-based methods using the Least Mean Square (LMS) error criterion; instead of knowing the source number, they iteratively extract peak sources from a fuzzy beamforming image, however, they tend to eliminate weak sources drowned in the background noise; besides, some important parameters such as attenuation factor, iteration number, have to be selected empirically. The Deconvolution Approach for Mapping of Acoustic Source (DAMAS) method [20] has been a breakthrough and is effectively applied in open wind tunnel tests by NASA. DAMAS gives an iterative solution of the system of linear equation under non-negative constraint, but DAMAS is sensitive to background noise and suffers from slow convergence. DAMAS2 and DAMAS3 [21] can accelerate the original DAMAS by confining the Point Spread Function (PSF) of antenna array to be shift invariant, but this assumption inevitably affects spatial resolution. The inverse methods [22, 23] overcome most of the drawbacks of the above methods, but they require huge computations and could not guarantee global optimum or stable solutions. For example, DAMAS with sparsity constraint (SC-DAMAS) [24] improves the DAMAS resolution, but is still not robust to noise interference. The Covariance Matrix Fitting (CMF) method [25] improves the robustness of SC-DAMAS by estimating the background noise, but it is not feasible for use in higher resolution imaging due to its huge dimensionality of variables. The ℓ_1-norm for enforcing sparsity and noise suppression are widely discussed in the literature, e.g. [26] and [27]. And paper [28] proposed to use the ℓ_1 norm with iteratively re-weighted least square methods for coherent/incoherent, distributed/multipole sources imaging. Above all, most of the inverse methods have to know some important parameter beforehand, or make necessary approximation on subspace separation. To overcome these constraints, the Bayesian inference approach via sparsity enforcing priors can obtain the most probably sparse solution, high spatial resolutions and robustness to the background noise [17, 29, 30], but unfortunately, Bayesian inference approach causes a great of computations. To summarize, all the above methods have excellent performances on some focused aspects, but most of them suffer one of the following drawbacks: poor spatial resolution, sensitivity to background noise, narrow dynamic range, a necessity for parameters and high computational cost.

In this paper, we aim to investigate aeroacoustic imaging with high spatial resolutions, wide dynamic range and moderat computational cost for near-field wide-band uncorrelated sources on the surface of static object in open wind tunnel tests based on the 2D NUA. In order to overcome most of mentioned drawbacks of the state-of-the-art

methods, the main idea of proposed approach is to explore the sparsity of spatial distributions of aeroacoustic sources. We propose a Robust super-resolution approach via Sparsity Constraint to estimate source powers and positions in poor SNR cases, and jointly estimate the variance of background noise. By simulations, experiment data and hybrid data, we then show en extended performance comparisons of proposed methods to conventional beamforming, CLEAN, DAMAS, Diagonal Removal DAMAS, SC-DAMAS and CMF methods.

The main novelties of this paper are 1) Robust deconvolution of the forward propagation model is proposed to jointly estimate sources and background noise by minimizing forward model errors, which could be regarded as unpredictable parts in the forward propagation model; 2) For super spatial resolution, the robust sparsity constraint is adaptively estimated by the sparsity of the spatial distribution of aeroacoustic sources. The advantages of the proposed approach are super spatial resolution, robustness to background noise, wide dynamic range of power estimations and normal computational cost. It can be applied for the near-field wide-band uncorrelated and extended aeroacoustic source imaging on the surface of the static object in open wind tunnel test based on the 2D non-uniform microphone array.

This paper is organized as follows. In Section 2 and Section 3, the forward propagation model of near-field wide-band acoustic sources and its classical inversion methods are briefly introduced. Then we propose our approach in Section 4. On simulations, Section 5 demonstrates performance comparisons of proposed method with state-of-the-art methods for the near-field wide-band monopole and extended source imaging. Results of the real data in open wind tunnel tests are illustrated in Section 6. In order to furthermore prove the effectiveness of proposed approach, Section 7 demonstrates its performances on hybrid data, in which some known synthetic sources are added to the real data. Finally the main conclusions of the paper are summarized in Section 8.

2. Forward propagation model of the near-field wide-band aeroacoustic source

2.1. Assumptions

Before modeling, we make three necessary assumptions on source natures, background noise and sensors:

- Aeroacoustic sources are spatially punctual (monopole) and uncorrelated, and locating on a plane;
- Background noise is Additive Gaussian White Noise (AGWN) with variance σ^2, mutually independent and identically distributed (i.i.d), and is also independent to sources;
- Sensors are omnidirectional with unitary gain.

2.2. Propagation model

We consider M microphone sensors and K (unknown) near-field wide-band sources, $\mathbf{s}^*$ at positions $\mathbf{P}^* = [\mathbf{p}_1^*, \cdots, \mathbf{p}_K^*]^T$ with $\mathbf{p}_k^*$ being 3D coordinate of kth real source. For each sensor, measured pressure signals are sampled, then discrete signals are divided into I blocks consisting of L snapshots, and the total number of measured samples is $T = I\,L$. Since the discrete signals are wide-band, the Discrete Fourier Transform (DFT) is applied to each block in order to obtain L narrow frequency bins. Thus the measured pressure signals $\mathbf{z}_i(f_l) = [z_{i,1}(f_l), \cdots, z_{i,M}(f_l)]^T$ for frequency f_l ($l \in [1, L]$) in the block $i \in [1, I]$ can be modeled as [19]:

$$\mathbf{z}_i(f_l) = \mathbf{A}^*(\mathbf{P}^*, f_l)\,\mathbf{s}_i^*(f_l) + \mathbf{e}_i(f_l)\,, \tag{1}$$

where $\mathbf{e}_i(f_l) = [e_{i,1}(f_l), \cdots, e_{i,M}(f_l)]^T$, $\mathbf{e}_i(f_l) \in \mathbb{C}^M$ denotes i.i.d AGWN noise; $\mathbf{s}_i^*(f_l) = [s_{i,1}^*(f_l), \cdots, s_{i,K}^*(f_l)]^T$, $\mathbf{s}_i^*(f_l) \in \mathbb{C}^K$ denotes the DFT of real source, $\mathbf{A}^*(\mathbf{P}^*, f_l) = [\mathbf{a}^*(\mathbf{p}_1^*, f_l), \cdots, \mathbf{a}(\mathbf{p}_K^*, f_l)]$, $\mathbf{A}^*(\mathbf{P}^*, f_l) \in \mathbb{C}^{M\times K}$ denotes the near-field steering matrix.

Unlike [19], we account for the ground reflection effect as discussed in authors' paper [29]. In Fig.1b, $\mathbf{a}^*(\mathbf{p}_k^*, f_l)$ is

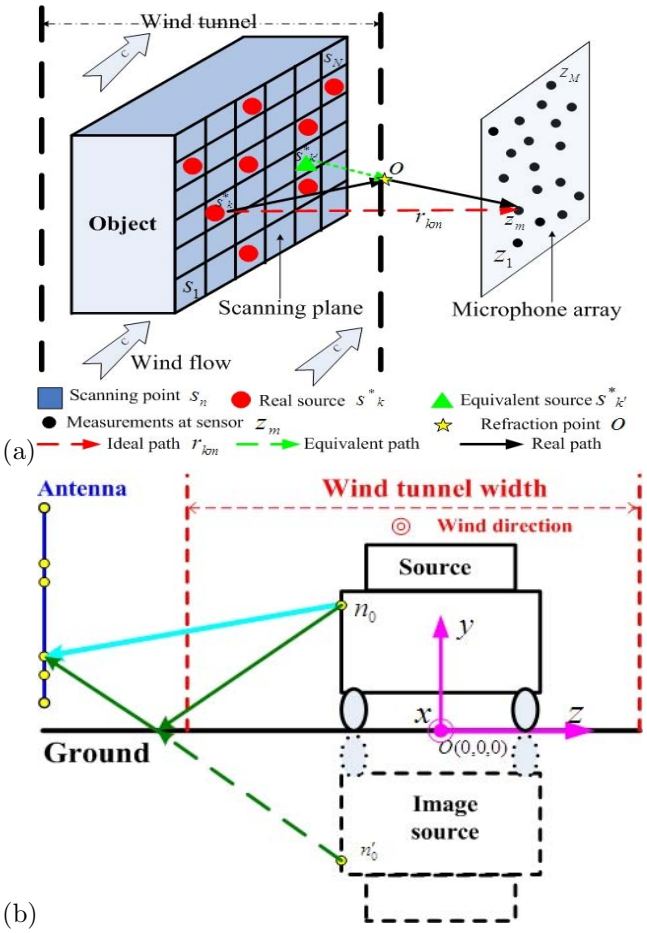

Figure 1: Illustration of open wind tunnel tests [29]: (a) configurations and acoustic refraction by wind, and (b) acoustic reflection on the ground.

composed by the direct propagation vector $\mathbf{a}_d^*(\mathbf{p}_k^*, f_l)$ and the ground reflection vector $\mathbf{a}_r^*(\mathbf{p}_{-k}^*, f_l)$:

$$\mathbf{a}^*(\mathbf{p}_k^*, f_l) = \mathbf{a}_d^*(\mathbf{p}_k^*, f_l) + \rho\, \mathbf{a}_r^*(\mathbf{p}_{-k}^*, f_l)\,, \tag{2}$$

where ρ denotes the reflecting coefficient ($0 \le \rho \le 1$), whose value mainly depends on ground conditions (material, temperature, humidity, etc.), and $\rho = 0.8$ is used in open wind tunnel experiments [7].

$\mathbf{a}_d^*(\mathbf{p}_k^*, f_l)$ is defined as:

$$\mathbf{a}_d^*(\mathbf{p}_k^*, f_l) = \left[\cdots, \frac{1}{r_{k,m}} \exp\left\{-j2\pi f_l \tau_{k,m}\right\}, \cdots\right]^T, \tag{3}$$

where $m = 1, \cdots, M$, $\tau_{m,k}$ is the propagation time from s_n^* to antenna m, and $r_{k,m}$ is the propagation distance during $\tau_{k,m}$.

Moreover, $\mathbf{a}_r^*(\mathbf{p}_{-k}^*, f_l)$ is defined as:

$$\mathbf{a}_r^*(\mathbf{p}_{-k}^*, f_l) = \left[\cdots, \frac{1}{r_{-k,m}} \exp\left\{-j2\pi f_l \tau_{-k,m}\right\}, \cdots\right]^T, \tag{4}$$

where $\mathbf{p}_{-k}^*$ denotes mirror positions of s_k^*, which is symmetric to the ground.

For the actual $r_{k,m}$, $r_{-k,m}$ and $\tau_{k,m}$, $\tau_{-k,m}$, we apply equivalent sources and mirror sources respectively to deal with the wind refraction and ground reflection, which are formulated in the Appendix of authors' paper [29].

3. Conventional solutions

The classical inverse problem is based on the discretization of the source plane, as illustrated in Fig.1a. The smaller grids are discretized, the higher spatial resolution could be achieved. Therefore the scanning plane is equally discretized into N ($N >> M > K$) scanning points $\mathbf{s}$ locating at $\mathbf{P}$, satisfying $\mathbf{P}^* \subset \mathbf{P}$. Each scanning point $\mathbf{s}_n$ could be regarded as a potential source, then in the space domain we have

$$\begin{cases} s_n = s_k^* & \text{for} \quad \mathbf{p}_n = \mathbf{p}_k^* \\ s_n = 0 & \text{for} \quad \mathbf{p}_n \neq \mathbf{p}_k^* \end{cases}. \tag{5}$$

From Eq.(5), $\mathbf{s}$ can be also expressed as

$$\mathbf{s} = [0, \cdots, s_1^*, 0, \cdots, s_k^*, 0, \cdots, s_K^*, 0, \cdots]_{N\times 1}\,. \tag{6}$$

Since the number K of real source $\mathbf{s}^*$ is limited and the number N of scanning points $\mathbf{s}$ is large enough, so that $\mathbf{s}$ is a sparse signal with K sparsity in the space domain. From now on, we will call $\mathbf{s}$ the sources, and $\mathbf{s}^*$ the real sources.

In Eq.(1), replacing $\mathbf{s}^*$ by $\mathbf{s}$ of Eq.(6), the propagation model with the discretization of the source plane can be expressed as:

$$\mathbf{z}_i(f_l) = \mathbf{A}(\mathbf{P}, f_l)\, \mathbf{s}_i(f_l) + \mathbf{e}_i(f_l)\,, \tag{7}$$

where $\mathbf{A}(\mathbf{P}, f_l) \in \mathbb{C}^{M\times N}$ is formed by the N steering vectors $\mathbf{a}(\mathbf{p}_n, f_l)$ similarly defined from Eq.(2):

$$\mathbf{a}(\mathbf{p}_n, f_l) = \mathbf{a}_d(\mathbf{p}_n, f_l) + \rho\, \mathbf{a}_r(\mathbf{p}_{-n}, f_l)\,, \tag{8}$$

where $\mathbf{a}_d(\mathbf{p}_n, f_l)$ and $\mathbf{a}_r(\mathbf{p}_{-n}, f_l)$ are defined from Eq.(3) and Eq.(4) by replacing $\mathbf{s}^*$ by $\mathbf{s}$.

3.1. Near-field beamforming

For the given location $\mathbf{p}_n$ and single frequency f_l, the steering vector $\mathbf{a}(\mathbf{p}_n, f_l)$ of Eq.(8) is shortened to $\mathbf{a}_n$. Let y_n denote the power estimation of the source s_n, thus y_n can be expressed by the conventional beamforming method as:

$$y_n = \frac{\tilde{\mathbf{a}}_n^H \hat{\mathbf{R}} \tilde{\mathbf{a}}_n}{\|\tilde{\mathbf{a}}_n\|_2^2}\,, \tag{9}$$

where the near-field beamforming coefficient $\tilde{\mathbf{a}}_n$ (the spatial filter coefficients) is obtained from Eq.(8) as:

$$\tilde{\mathbf{a}}_n = \frac{\mathbf{a}_n}{||\mathbf{a}_n||_2^2}\,. \tag{10}$$

In Eq.(9), $\hat{\mathbf{R}}$ is short for $\hat{\mathbf{R}}(f_l)$, which denotes the estimation of measured cross spectrum $\mathbf{R}$. In practice, $\hat{\mathbf{R}}$ is estimated by:

$$\hat{\mathbf{R}} = \frac{1}{I}\sum_{i=1}^{I} \mathbf{z}_i(f_l)\mathbf{z}_i(f_l)^H\,. \tag{11}$$

According to the discretized propagation model in Eq.(7) and the assumptions in subsection 2.1, $\mathbf{R}$ is modeled by

$$\mathbf{R} = \mathbb{E}\{\mathbf{z}_i(f_l)\mathbf{z}_i(f_l)^H\} = \mathbf{A}\mathbf{X}\mathbf{A}^H + \sigma^2\mathbf{I}_M\,, \tag{12}$$

where σ^2 is the variance of the i.i.d AGWN noise; $\mathbf{I}_M$ is the $M \times M$ identity matrix; and the cross spectrum matrix $\mathbf{X}$ of the source $\mathbf{s}$ is defined as $\mathbf{X} = \mathbb{E}\{\mathbf{s}\mathbf{s}^H\}$. For uncorrelated sources $\mathbf{s}$, $\mathbf{X}$ is diagonal with its diagonal items $\mathbf{x} = \mathrm{diag}\,[\mathbf{X}]$ standing for source powers.

3.2. Near-field DAMAS method and its improved versions

Based on the near-field beamforming of Eq.(9), $\hat{\mathbf{R}}$ of Eq.(11) is known to converge to $\mathbf{R}$ of Eq.(12) when the block number I is large enough, namely $\hat{\mathbf{R}} \approx \mathbf{R}$ for $I >> 1$. Then introduce Eq.(12) into Eq.(9) and match the following conditions: block number is large enough ($I >> 1$); sources are uncorrelated ($\mathbf{X}$ is diagonal); noise is negligible ($\sigma^2 = 0$), we then obtain the following inverse problem, which can be solved by the DAMAS approach [20]:

$$y_n = \frac{\tilde{\mathbf{a}}_n^H \hat{\mathbf{R}} \tilde{\mathbf{a}}_n}{\|\tilde{\mathbf{a}}_n\|_2^2} \approx \sum_{q=1}^{N} c_{n,q}\, x_q\,, \tag{13}$$

where x_q denotes the power of source s_q, with $q = 1, \cdots, N$; and $c_{n,q}$ denotes the array response as:

$$c_{n,q} = \frac{\|\tilde{\mathbf{a}}_n^H \mathbf{a}_q\|_2^2}{\|\tilde{\mathbf{a}}_n\|_2^2}\,. \tag{14}$$

Notice that Eq.(13) shows that the Beamforming estimated power y_n for x_n depends on the powers of all $\mathbf{x}$, except when the microphone array aperture is large enough, the array response approximates the Dirac function, namely $c_{n,q} \approx \delta_{n,q}$, thus $y_n = x_n$; but in practice, this condition is not verified and Eq.(13) is the expression of the inverse problem. For $\mathbf{x} = [x_1, \cdots, x_N]^T$, $\mathbf{x} \in \mathbb{R}^N$, Eq.(13) can be written in vectorial form as:

$$\mathbf{y} \approx \mathbf{C}\mathbf{x}\,, \tag{15}$$

where $\mathbf{y} = [y_1, \cdots, y_N]^T$, $\mathbf{y} \in \mathbb{R}^N$, and the power transferring matrix $\mathbf{C} \in \mathbb{R}^{N\times N}$ has the coefficient $c_{n,q}$ of Eq.(14).

For the present aeroacoustic problems, $\mathbf{C}$ is often singular as discussed in [20, 31]. Therefore DAMAS iteratively solves the linear system of Eq.(15) with non-negative constraint ($\mathbf{x} \geq 0$). And DAMAS has been proved to be a powerful method to deconvolve the beamforming result and has been successfully used by NASA [20]. However, it is not robust to the background noise due to assuming $\sigma^2 = 0$ and suffers from slow convergence. Several methods have improved its robustness. Diagonal Removal (DR) DAMAS [20] constrains $\mathrm{diag}\left[\hat{R}\right] = 0$ to suppress background noise interference, but DR technique harms weak sources; the SC-DAMAS [24] method investigates sparsity constraint for super spatial resolution, but it is still sensitive to noise. Instead of deconvolving the beamforming result, the CMF with sparsity constraint [25] directly estimates measured covariance matrix $\mathbf{R}$ and noise variance σ^2; However, CMF suffers from slow convergence; To accelerate DAMAS in the far-field field, $\mathbf{C}$ could be approximated by a Toeplitz Block Toeplitz (TBT) matrix,

therefore DAMAS2 and DAMAS3 [21] are proposed, but their spatial resolutions are inevitably deteriorated , especially applied in the near-field case.

3.3. Classical inverse solutions

In order to improve the robustness and obtain super resolution from Eq.(15), classical inverse methods aim to minimize both data fitting part and regularization part under the non-negative constraint as follows:

$$\begin{cases} \mathbf{x} = \arg\min_{\mathbf{x}} \left\{ ||\mathbf{y} - \mathbf{C}\mathbf{x}||_2^2 + \alpha ||\mathbf{x}||_p^p \right\} \\ \text{s.t.} \quad \mathbf{x} \succeq 0 \end{cases} . \tag{16}$$

For the regularization form $\|\cdot\|_p$, when $p = 0$, it refers to the real sparse regularization $||\mathbf{x}||_0$, but unfortunately it is an NP hard optimization problem. However, $||\mathbf{x}||_0$ can be approximately solved by the Iterative Hard Thresholds (IHT) method in [32]. When $p = 1$, equation (16) involves the ℓ_1 norm, and it is solved by the LASSO in [33], atomic decomposition by basis pursuit in [34] and the iterative thresholds method in [35]. When $0 < p < 1$, it corresponds to the Iterative Reweighed algorithm using ϵ-regularization strategy discussed in [36], which obtains sparser result than the ℓ_1. But equation (16) with ℓ_p, $p \in (0, 1)$ is a nonconvex optimization problem.

For the regularization parameter α, the paper [37] argued that α should be proportional to the inverse of the SNR; while paper [34] indicated that $\alpha = \sigma\sqrt{2log(M)}$ with M being the number of antenna; In paper [38], optimal Tikhonov regularization parameter is selected by the Generalized Cross Validation and L-curve method. But Tikhonov regularization could not provide estimations as sparse as the ℓ_1 norm does. Above all, classical methods show that regularization parameter is essential to Eq.(16), but parameter selection depends on the priors like SNR or noise level, and it inevitably causes extra unexpected computations.

Classical sparsity method or Compressed Sensing (CS) discussed in [39, 40] aims to solve

$$\begin{cases} \hat{\mathbf{x}} = \arg\min_{\mathbf{x}} \{||\mathbf{x}||_1\} \\ \text{s.t.} \quad \mathbf{y} = \mathbf{C}\mathbf{x}, \quad \mathbf{x} \succeq 0 \end{cases} . \tag{17}$$

However, due to the large dimension of linear equation constraint $\mathbf{y} = \mathbf{C}\mathbf{x}$, Eq.(17) is too time-consuming to solve. Moreover, it is sensitive to background noise because of noise-free assumption in the original DAMAS method.

4. Proposed approach

4.1. Proposed forward model of power propagation

When modeling the inverse problem for Eq.(7), Eq.(12) or Eq.(15), most of the classical methods did not directly consider the background noise existing at the antenna array. Recently, papers [41] and [42] proposed the Spectral Estimation Method (SEM) to improve robustness. They applied a known reference noise regarded as the estimation of background noise for open wind tunnel tests. But this reference noise could not always be obtained beforehand. A subspace approach using the Oblique Projector (OP) technique for uncorrelated and colored noise suppression is discussed in [43]. The OP technique is more robust than the Diagonal Removal used in DR-DAMAS method [20], but it relies on the rank of the rank-deficient covariance matrix of correlated noises, which increases the complexity.

Here we take into account the background noise in Eq.(12) and explore the independence between sources and noise; comparing to Eq.(15), we then get the improved forward model as follows:

$$\mathbf{y} = \mathbf{C}\mathbf{x} + \sigma^2 1_N + \xi\,, \tag{18}$$

where $1_N = [1, \cdots, 1]_{N\times 1}$; and $\xi = [\xi_1, \cdots, \xi_N]$ denotes the model error, which represents unpredictable parts in the forward model of Eq.(15).

4.2. Proposed Robust super-resolution approach with sparsity constraint (SC-RDAMAS)

Many state-of-the-art methods like [44–46] are developed to improve the Eq.(17) for robust, effective and fast sparse solutions. Instead of establishing complicate mathematical model, we investigate a direct and effective modification of Eq.(17) by applying the proposed forward model of Eq.(18) and the sparsity of source spatial distribution. Considering the sparsity fact, aeroacoustic sources sparsely lay on the surface of the object. Taking the vehicle in the open wind tunnel test for example, most of sources sparsely locate on the rearview mirrors and around the wheels. Comparing to the number of scanning points, the number of real sources is much fewer; and the total power of real sources is limited and unchanged, no matter how to discretize the source plane.

Therefore our proposed approach aims to solve Eq.(18) as follows:

$$\begin{cases} (\hat{\mathbf{x}}, \hat{\sigma^2}) = \arg\min_{(\mathbf{x},\sigma^2)} \left\{ \mathcal{J}(\mathbf{x}, \sigma^2) \right\} \ with \\ \mathcal{J}(\mathbf{x}, \sigma^2) = ||\mathbf{y} - \mathbf{C}\mathbf{x} - \sigma^2 1_N||_2^2 \\ \text{s.t.} \quad \mathbf{x} \succeq 0, \quad \|\mathbf{x}\|_1 \leq \beta, \quad \sigma^2 \geq 0 \end{cases} , \tag{19}$$

Where β denotes the total source powers, which is defined as:

$$\beta = \sum_{k=1}^{K} x_k^* = \|\mathbf{x}^*\|_1 , \tag{20}$$

where K denotes the real source number, and real source powers $\mathbf{x}^*$ are defined as $\mathbf{x}^* = \text{diag}\left[E[\mathbf{s}^*\mathbf{s}^{*H}]\right]$ with real sources $\mathbf{s}^* = [{s^*}_1, \cdots, {s^*}_K]^T$.

4.2.1. Estimation of sparsity parameter β

The source powers $\mathbf{x}$ obtained from Eq.(12) has the relationship with real source powers $\mathbf{x}^*$ in Eq.(20) as follows:

$$x_n = \begin{cases} {x^*}_k & \text{for} \quad \mathbf{p}_n = \mathbf{p}_k \\ 0 & \text{for} \quad \mathbf{p}_n \neq \mathbf{p}_k \end{cases} , \tag{21}$$

Where $\mathbf{p}_n$ and $\mathbf{p}_k$ denotes the 3D coordinates of scanning point n and real source k respectively. Therefore $\mathbf{x}$ is as a sparse signal in spatial domain as $\mathbf{s}$ defined in Eq.(6).

Therefore we take $\beta \geq \|\mathbf{x}\|_1 = \|\mathbf{x}^*\|_1$ for the sparsity constraint on total source powers. If β is too large, the estimated $\hat{\mathbf{x}}$ would be more dispersed than expected; if too small, some weak sources would be lost. To determine β, an useful technique [24] is to normalize each column of the steering matrix $\mathbf{A}$ in Eq.(7).

Here we apply this techique for general cases. Let

$$\mathbf{A}' = \left[\frac{\mathbf{a}_1}{||\mathbf{a}_1||}, \cdots, \frac{\mathbf{a}_N}{||\mathbf{a}_N||} \right] , \tag{22}$$

namely $\mathbf{A}'$ is obtained from the $\mathbf{A}$ column-normalized by $||\mathbf{a}_n||$; therefore $\mathbf{A}'$ satisfies $\text{diag}\left[{\mathbf{A}'}^H\mathbf{A}'\right] = 1_N$. This means that column-normalized propagation matrix $\mathbf{A}'$ keeps the total source powers unchanged.

According to Eq.(12), we have

$$\text{tr}\left\{\mathbf{R}'\right\} = \text{tr}\left\{\mathbf{A}'\mathbf{X}{\mathbf{A}'}^H + \sigma^2\mathbf{I}\right\} = \text{tr}\left\{{\mathbf{A}'}^H\mathbf{A}'\mathbf{X}^H\right\} + \sigma^2\text{tr}\left\{\mathbf{I}'_N\right\} , \tag{23}$$

where $\text{tr}\left\{\cdot\right\}$ denotes matrix trace; $\mathbf{R}'$ is obtained from $\mathbf{R}$ column-normalized by $||\mathbf{a}_n||^2$; $\mathbf{I}'_N$ is obtained from $\mathbf{I}_N$ column-normalized by $||\mathbf{a}_n||^2$. According to the definition of $\mathbf{A}'$ in Eq.(22) and $x_n \geq 0$, we have

$$\text{tr}\left\{{\mathbf{A}'}^H\mathbf{A}'\mathbf{X}^H\right\} = \sum_{n=1}^{N} x_n = ||\mathbf{x}||_1 . \tag{24}$$

Since $\mathbf{R}$ is Hermitian, it can be diagonalized into

$$\mathbf{R} = \mathbf{U}\mathbf{\Lambda}\mathbf{U}^H , \tag{25}$$

where $\mathbf{U}$ is the unitary matrix, whose columns are eigenvectors of $\mathbf{R}$, and $\mathbf{\Lambda}$ is the eigenvalue matrix of $\mathbf{R}$, with diagonal items $\lambda_1 \geq \lambda_2 \geq \cdots \geq \lambda_K \geq \lambda_{K+1} = \cdots = \lambda_M = \sigma^2$. By column normalization, we similarly have

$$\text{tr}\left\{\mathbf{R}'\right\} = \text{tr}\left\{\mathbf{U}\mathbf{\Lambda}'\mathbf{U}^H\right\} = \text{tr}\left\{\mathbf{\Lambda}'\right\} , \tag{26}$$

Where $\mathbf{\Lambda}'$ is obtained from $\mathbf{\Lambda}$ column-normalized by $||\mathbf{a}_n||^2$ in Eq.(25).

According to Eqs.(20), (23), (24) and (26), β is modeled by

$$\beta = \text{tr}\left\{\mathbf{\Lambda}'\right\} - \sigma^2\text{tr}\left\{\mathbf{I}'_N\right\} , \tag{27}$$

where β is the function of noise variance σ^2. In our proposed approach, β is estimated by

$$\hat{\beta} = \mathrm{tr}\left\{\hat{\mathbf{\Lambda}}'\right\} - \hat{\sigma^2}\mathrm{tr}\left\{\mathbf{I}'_N\right\}, \tag{28}$$

where $\hat{\mathbf{\Lambda}}'$ is obtained by $\hat{\mathbf{R}}' = \hat{\mathbf{U}}\hat{\mathbf{\Lambda}}'\hat{\mathbf{U}}^H$, with $\hat{\mathbf{R}}$ being estimated by Eq.(11) and $\hat{\mathbf{R}}'$ obtained from $\hat{\mathbf{R}}$ column-normalized by $||\mathbf{a}_n||^2$. In practise, $\hat{\sigma^2} = \min\{\lambda_m\}_{m=1}^{M}$ is used by paper [24]; And a better initialization [25] is as follows:

$$\hat{\sigma^2} = \frac{1}{M - \hat{K} + 1}\sum_{m=\hat{K}+1}^{M}\lambda_m \tag{29}$$

where $\hat{K}$ is the estimated source number. Finally, total source power β depends on the source number K.

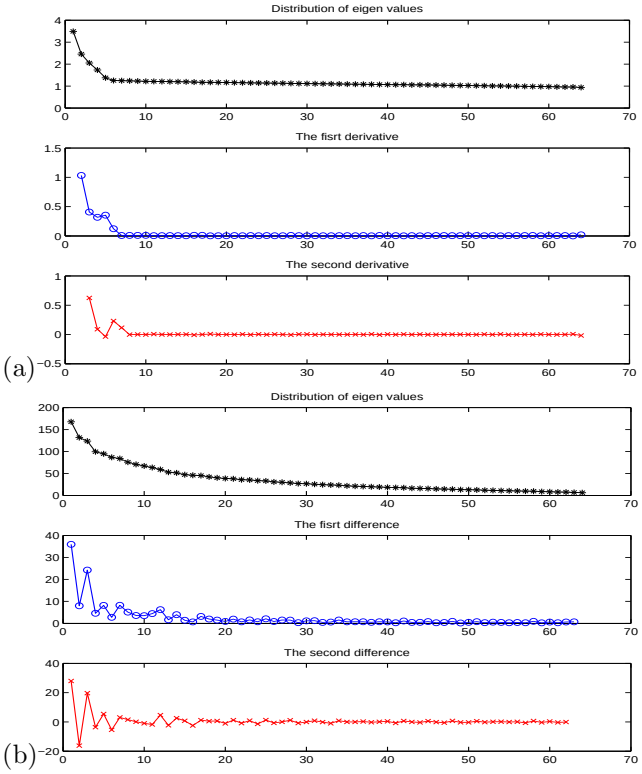

Figure 2: Eigenvalue distribution $\lambda(m)$, first-order $(-d'\lambda(m))$ and second-order $(-d''\lambda(m))$ derivatives (from ceiling to bottom) at 2500Hz, y-axis $\lambda(m)$, x-axis $m = 1, \cdots, M$; (a) 5 uncorrelated monopole sources at $SNR = 0dB$ and (b) Real data

For $\hat{K}$, our proposed SC-RDAMAS approach applies the property of eigenvalue distribution for better initialization. Let $\lambda(m)$ with $m = 1, \cdots, M$ denote the eigenvalue distribution of $\mathbf{R}$. Since $\lambda(m)$ is a non-increasing function, the second-order derivative $d''[\lambda(m)]$ describes the change of decreasing rate of $\lambda(m)$. From certain point $\hat{K}$ on $(m \geq \hat{K})$, the change of decreasing rate approaches zero $(d''[\lambda(m)] \approx 0)$. Therefore this $\hat{K}$ can be regarded as the estimation of K. This conclusion could be explained by the sparsity fact that $\lambda(m)$ has much fewer number of source powers $(2K < M << N)$ than that of noise powers; and noise powers are not greatly distinct from each other, particularly for AWGN noise; therefore the curve of eigenvalue distribution has a short and steep head, and a long and smooth tail, which are illustrated in Fig.2 for simulated and real data respectively.

4.2.2. Proposed alternative solution

In Eq.(19), our proposed approach is a convex quadratic minimization under linear matrix constraints, which can be solved by interior point methods using MATLAB toolbox SeMuDi [47]. In order to improve the robustness of sparsity constraint, we propose an alternative solution to estimate source powers $\mathbf{x}$ and noise σ^2 for a given source number K, then renew K for better estimation of $\mathbf{x}$ and σ^2. The main steps of the proposed algorithm are depicted as follows:

- Step 1: $\hat{K}^{(1)}$ is initialized by eigenvalue distribution, and $\hat{\mathbf{x}}^{(1)} = 0$;
- Step 2: $\hat{\sigma^2}^{(k)}$ is obtained by Eq.(29), then $\hat{\beta}^{(k)}$ by Eq.(28);
- Step 3: $(\hat{\mathbf{x}}^{(k+1)}, \hat{\sigma^2}^{(k+1)}) = \arg\min_{(\mathbf{x},\sigma^2)}\left\{\mathcal{J}(\hat{\mathbf{x}}^{(k)}, \hat{\sigma^2}^{(k)})\right\}$ with sparsity constraint in Eq.(19);
- Step 4: If $\mathcal{J}(\hat{\mathbf{x}}^{(k+1)}, \hat{\sigma^2}^{(k+1)})$ has significant diference from $\mathcal{J}(\hat{\mathbf{x}}^{(k)}, \hat{\sigma^2}^{(k)})$, then do Step 5; if not, do Step 6;
- Step 5: $\hat{K}^{(k+1)} = \hat{K}^{(k)} + 1$, and repeat Step 2-4;
- Step 6: Stop the iterations.

4.3. Wide-band results

In the open wind tunnel experiments, aeroacoustic sources are generated by the friction between the car and wind flow. Physically, different car parts with various sizes produce vibrations with different frequencies. Therefore aeroacoustic sources are wide-band signals. We consider the frequency range $[f_{min}, f_{max}]$ consisting of L frequency bins. Let $\hat{\mathbf{x}}(f_l)$ be the estimation of $\mathbf{x}(f_l)$ in lth frequency bin. Then total power $\mathbf{x_{wb}}$ over wide-band $[f_{min}, f_{max}]$ can be estimated by

$$\hat{\mathbf{x}}_{\mathbf{wb}} = \sum_{f_l=f_{min}}^{f_{max}} \hat{\mathbf{x}}(f_l)\,. \tag{30}$$

5. Simulated data

This section demonstrates the performances of the proposed approach for near-field aeroacoustic imaging in the poor SNR case. Proposed approach is compared with conventional beamforming, CLEAN, DAMAS, DR-DAMAS, SC-DAMAS and CMF methods. Results are presented on images which represents the source power (dB) and their localization. In addition, section profiles are shown on the edge of the images. We use two criteria to quantitatively evaluate the power estimation accuracy. One is the average estimation error of real source power $\overline{\Delta x^*}$:

$$\overline{\Delta x^*} = \frac{1}{K}\sum_{k=1}^{K} |\hat{x^*}_k - x^*_k|\,, \tag{31}$$

where real source powers $\mathbf{x}^* = [x^*_1, \cdots, x^*_K]$ are obtained by $\mathbf{x}^* = \text{diag}\left[\mathbb{E}\{\mathbf{s}^*\mathbf{s}^{*H}\}\right]$. $\overline{\Delta x^*}$ can reflect estimation performance of source powers. The other is the power image reconstruction relative error δ_i, with $i = 1, 2$ defined as:

$$\delta_i = \frac{\|\hat{\mathbf{x}} - \mathbf{x}\|_i^i}{\|\mathbf{x}\|_i^i}\,. \tag{32}$$

δ_i can reflect the reconstruction performance of power image.

5.1. Configurations

The general configuration used to generate synthetic data is based on the experiment carried out by Renault

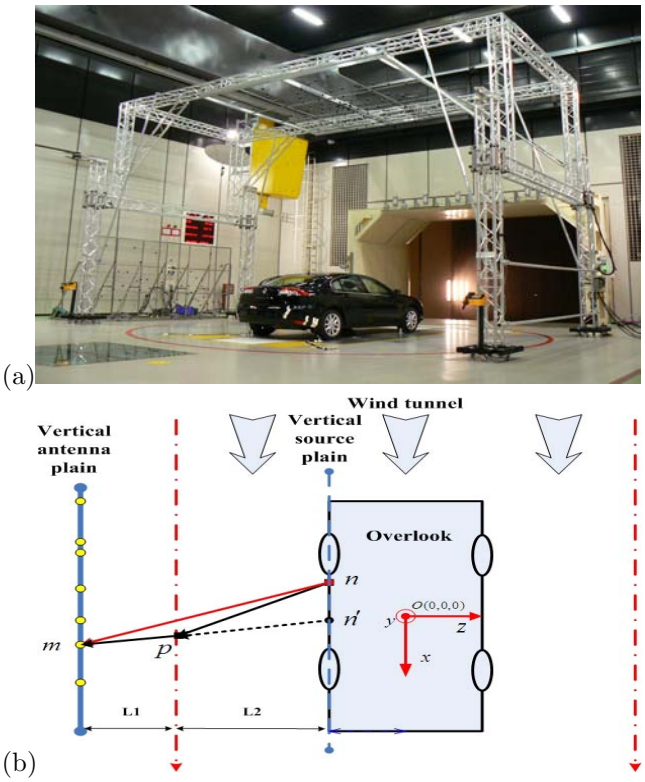

Figure 3: Configurations of open wind tunnel S2A: (a) open wind tunnel S2A [7] and (b) overlook and acoustic refraction[29]

SAS [7] as shown in Fig.3. The distance between the antenna plane and source plane is around $D = 4.50m$. There are 64 non-uniform antenna (NUA) located at $2m \times 4m$ in the vertical plane, whose horizontal aperture is longer than the vertical, as shown in Fig.3a. The average aperture of antenna array is $d = 2m$. The aeroacoustic propagation speed in the open air is $c_0 \approx 340m/s$. The total number of snapshots is $T = 10000$. As plotted in Fig.4a, we have simulated 4 monopole sources and 5 extended sources with different patterns, and the source number is $K = 23$; their powers are $[0.08, 2]$ ($[-10.37, 3.7]dB$) with $14dB$ dynamic range. The background noise variance is $\sigma^2 = 0.86$ ($-0.7dB$). And the average SNR is $0dB$.

Some parameters should be selected carefully, like frequency range and scanning step Δx_p. The near-field condition is guaranteed by $D < d^2/(4\lambda)$ for any $f > 1500Hz$. Since the spatial resolution of beamforming at $f = 2500Hz$ is $\Delta B \approx \lambda R/d = 31cm$, the selected scanning step $\Delta x_p =$

$5cm$ satisfies $\Delta x_p/\Delta B < 0.2$ for any $f < 3500Hz$, which avoids the spatial aliasing problem as discussed in the DAMAS [20]. Therefore the scanning region is of 20×30 pixels. Since the scanning point number $N = 600$ is large enough to source number $K = 23$, the simulated source $\boldsymbol{s}$ is the sparse signal.

5.2. Results

As shown in Fig.4, the beamforming merely gives a very fussy result of several main sources. Both the DAMAS with 5000 iterations (5000i), CLEAN and SC-DAMAS are too sensitive to provide reliable results in strong background noise. The DR-DAMAS removes the noise and roughly estimates the extended source, but it loses some of weak sources. The CMF well estimates the noise variance, however it also fails to reconstruct weak sources. According to $\overline{\Delta x^*}$ and δ_i in the Table 1 and Table 2, the proposed SC-RDAMAS approach works better than the others. It well detects each pattern of extended source, and better estimates source powers in poor SNR situation.

In Fig.5, we show the robustness to background noise of mentioned methods in the SNR from -6dB to 18 dB. Proposed method well outperforms the other methods, since in very poor SNR cases it still achieves very small power image reconstruction relative errors δ_1 and δ_2.

In Fig.6, we show the performance comparison of wideband simulated data from $1600Hz$ to $2600Hz$ at $SNR = 3dB$. With the higher frequencies, all the methods can obtain better spatial resolutions, but our proposed methods achieves the most significant improvements.

In Fig.7, it reveals the influence of estimated source number in the SC-DAMAS method and our proposed SC-RDAMAS at $SNR = 0dB$, $f = 2500Hz$. The real source number is $K \in [9, 13]$. Both of the two methods apply the sparsity constraint. For the SC-DAMAS method, source number affects greatly the power image reconstruction relative error δ_i; but for the proposed approach, under estimation of source number ($\hat{K} < 9$) significantly affects δ_i,

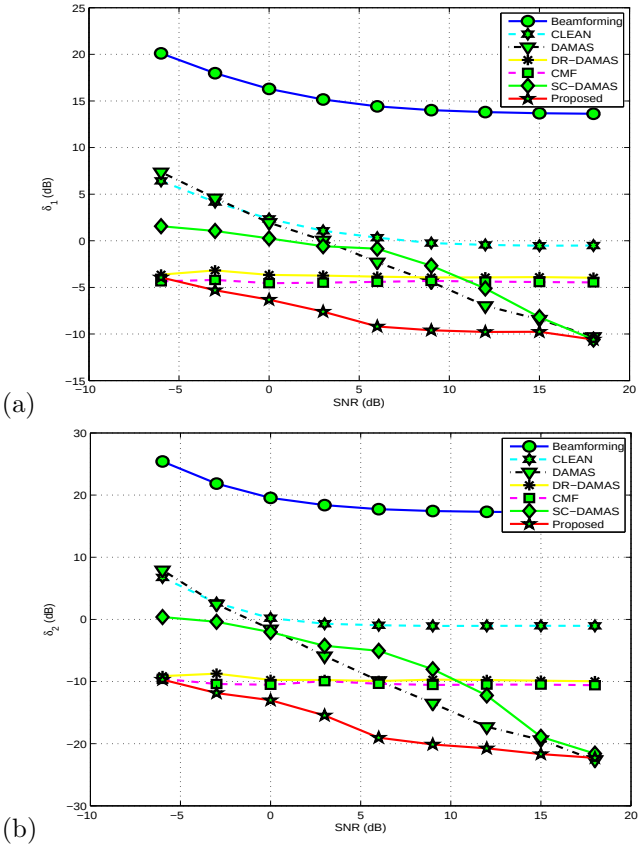

Figure 5: Performance comparison of power image reconstruction relative errors δ_1 and δ_2 within $SNR \in [-6, 18]dB$ at $f = 2500Hz$ on simulations: (a) δ_1 VS SNR (dB) and (b) δ_2 VS SNR (dB).

but over-estimation ($\hat{K} > 13$) does not affect at all, since proposed SC-RDAMAS can adaptively estimate the source number K, and alternatively estimates the noise variance σ^2 and total power of sources β according to Eq.(19).

6. Wind tunnel experiments

Nowadays both the consumers and producers pay more and more attentions to the aeroacoustic comfort of various human transportation: automobiles, aircraft, trains and ferries etc. The open wind tunnel experiments carried out by Renault SAS [7] intends to measure the aeroacoustic influence on the passersby, the drivers and passengers when Renault cars travel on the high-way.

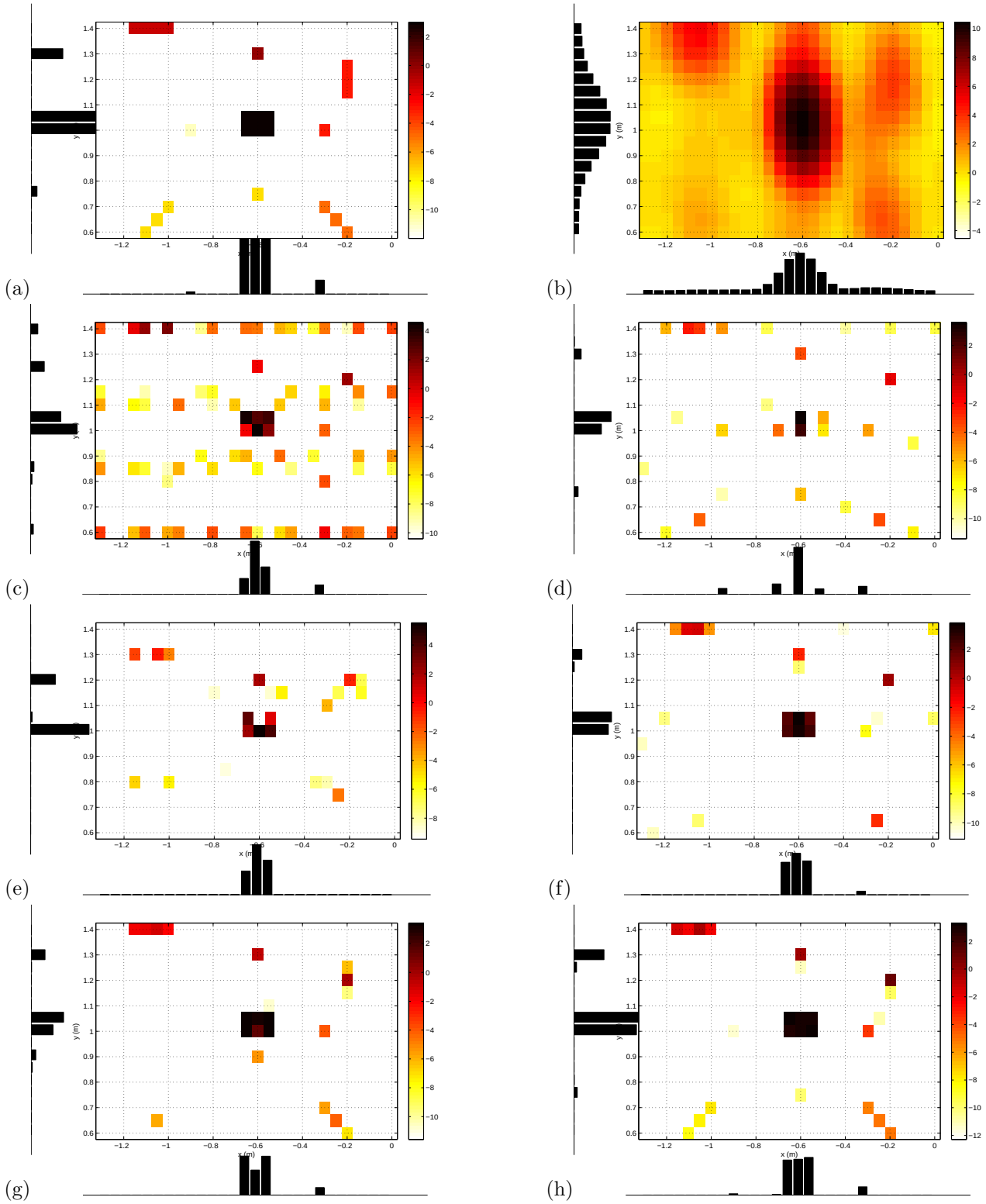

Figure 4: Simulation on extended source imaging at $2500Hz$, real $\sigma^2 = 0.86$, $SNR = 0\ dB$ and $14dB$ dynamic range; (a) 5 extended sources and 4 monopoles (b) Beamforming (c) DAMAS with 5000 iterations (5000i) (d) CLEAN (e) SC-DAMAS (f) DR-DAMAS (5000i) (g) CMF and (h) Proposed SC-RDAMAS

Table 1: Power estimations of 4 monopole sources at $2500Hz$, SNR=$0dB$, dynamic range $14dB$, with $\overline{\Delta x^*}$ averaged power estimation error, $\delta_{1,2}$ power image reconstruction relative errors and $\hat{\sigma^2}$ estimated noise covariance, a cell containing '-' means unavailable.

Source powers	0.08	0.18	0.98	0.50	$\overline{\Delta x^*}$	δ_1	δ_2	$\hat{\sigma^2}$ ($\sigma^2 = 0.86$)
Beamforming	1.57	11.28	3.51	2.02	4.16	69.64	121.93	-
DAMAS	-	-	-	0.44	0.33	3.14	1.33	-
SC-DAMAS	-	-	-	-	-	1.03	0.58	-
CLEAN	-	0.25	0.44	0.28	0.23	0.87	0.67	-
DR-DAMAS	-	-	0.77	0.23	0.19	0.30	0.08	-
CMF	0.09	-	0.80	0.40	0.12	0.31	0.10	0.89
Proposed	0.09	0.10	1.05	0.43	0.06	0.21	0.06	0.85

Table 2: Power estimations of the extended source on the center of image at $2500Hz$, SNR=$0dB$, with $\overline{\Delta x^*}$ averaged power estimation error, a cell containing '-' means unavailable.

Source powers	2.00	2.00	2.00	2.00	2.00	2.00	$\overline{\Delta x^*}$
Beamforming	2.64	9.60	9.70	9.64	11.34	9.77	6.78
DAMAS	4.50	1.25	0.48	2.54	0.49	1.88	1.15
CLEAN	2.29	0.37	1.69	-	0.27	0.34	1.27
SC-DAMAS	1.68	2.49	1.16	0.10	2.23	0.65	0.75
CMF	1.36	2.86	2.07	2.09	1.92	1.05	0.45
DR-DAMAS	2.15	2.05	1.82	1.83	2.50	1.45	0.27
Proposed	1.83	2.00	2.05	1.72	2.16	1.95	0.12

6.1. Configurations

Figure 3 shows the open wind tunnel S2A [7], the vehicle, NUA array and the wind refraction. We suppose that all aeroacoustic sources locate on the same plane. This assumption is almost satisfied, because the curvature of the car side is relatively small compared to the distance $D = 4.5$ between the car side and the sensor plane. The smaller scanning region has 20×30 pixels; the larger one 30×100 pixels, with scanning step $\Delta x_p = 5cm$. There are $T = 524288$ snapshots, $I = 204$ blocks, $L = 2560$ snapshots per bloc. The working frequency band is $[2400, 2600]Hz$, and sampling frequency $f_s = 2.56 \times 10^4$ Hz. The image results are shown by normalized dB images with $10dB$ span.

For the actual propagation time $\tau_{n,m}$ and distance $r_{n,m}$ defined in Eq.(3), we apply equivalent source to make propagation correction of the refraction: for antenna m, it seems to receive the signal from equivalent source $s_{n'}$ instead of original source s_n along a direct path $r_{n',m}$ during the same propagation time $\tau_{n',m}$, as if there is no wind influence in the open wind tunnel, as shown in Fig.3b. For $\tau_{n,m}$ and $r_{n,m}$ defined in Eq.(3), we use the mirror source s_{-n} to correct the ground reflection. The details of the propagation correction is discussed in authors' paper [29].

6.2. Results of single frequency

For aeroacoustic imaging on the car side, the Fig.8 illustrates the normalized estimated power images of vari-

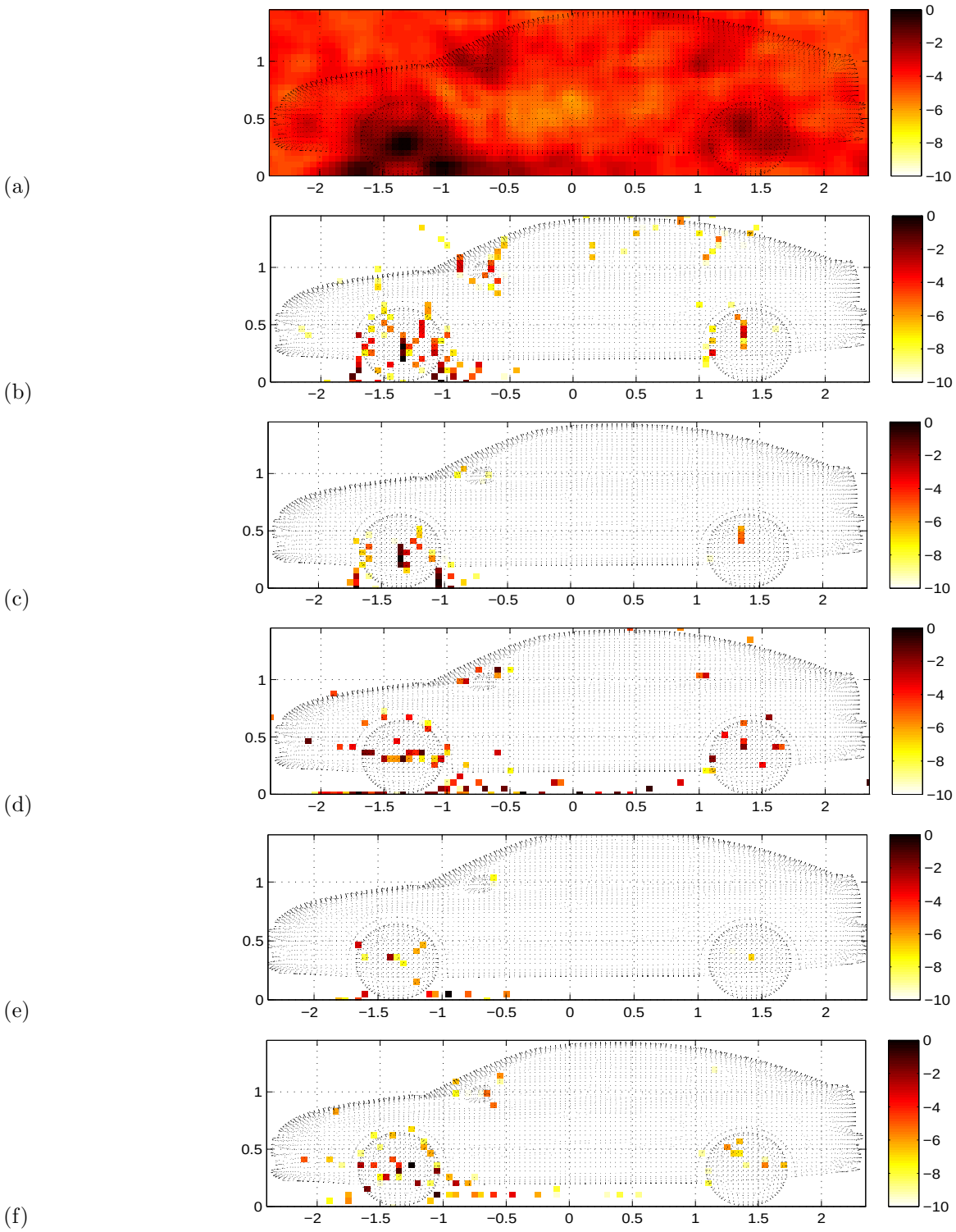

Figure 8: Acoustic imaging of the whole vehicle at $2500Hz$: (a) Beamforming (b) DAMAS (5000i) (c) DR-DAMAS (5000i) (d) CLEAN (e) SC-DAMAS and (f) Proposed SC-RDAMAS.

Table 3: Computational cost of acoustic imaging at $2500Hz$ for vehicle side with sizes $135cm \times 470cm$, $5cm$ interval, 27×94 image, based on CPU:3.33GHz.

Methods	Beamforming	DAMAS (5000i)	DR-DAMAS (5000i)	CLEAN	Proposed	SC-DAMAS	CMF
Time (s)	1	10	11	45	852	1254	Very Long

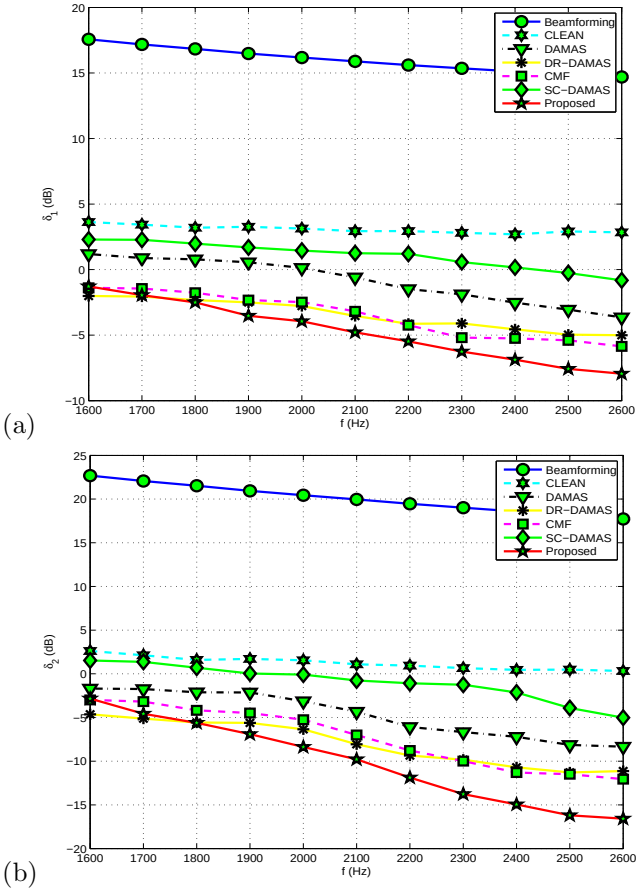

Figure 6: Performance comparison of δ_1 and δ_2 within wide-band $[1600, 2600]Hz$ at $SNR = 3dB$ on simulations: (a) δ_1 (dB) VS f (Hz) and (b) δ_2 (dB) VS f (Hz).

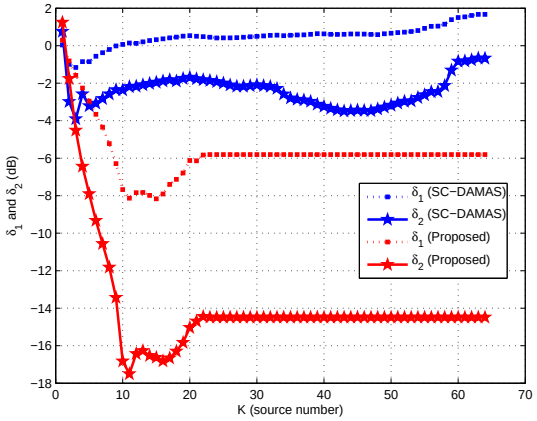

Figure 7: Robustness comparison of δ_i within different estimated source number $\hat{K}$ between the SC-DAMAS method and proposed approach at $SNR = 3dB$.

ous methods at $2500Hz$ with $10dB$ span. The beamforming merely gives the fuzzy image of strong sources around the front wheel, rearview mirror and back wheel as seen in Fig.8a; in Fig.8b, DAMAS well deconvolves the beamforming image, and discovers weak sources on the front light, front cover and side windows; however, DAMAS gets many false targets on the air; the DR-DAMAS eliminates most of the false targets, but it also harms weak sources as shown in Fig.8c; both Fig.8d and Fig.8e show that both CLEAN and SC-DAMAS can overcome drawbacks of the DAMAS, but unexpected strong points are detected on the ground or in the air; finally in Fig.8f, the proposed SC-RDAMAS obtains a better result than the others, especially on the profiles of two wheels and rearview mirror. Furthermore, the consuming time of different methods are given in Table 3. In our proposed approach, adaptively estimating the sparsity constraint increases the computational burden, but it still remains a moderate computing cost among the mentioned methods.

Based on the results of the car side, we furthermore investigate the details of local parts. Taking the rearview mirror for example, the beamforming in Fig.9a principally demonstrates 3 groups of sources: one on the corner of the front wheel, two on the rearview mirror; DAMAS in Fig.9b improves the resolution of the beamforming, but it also gets many dirty spots, most of which are removed by DR-DAMAS in Fig.9c; CMF in Fig.9d obtains better

results and discovers extra sources on the corner of the front cover and front window, but there are still some false alarms; SC-DAMAS in Fig.9e achieves a result as good as CMF does; the proposed approach in Fig.9f achieves more accurate estimations of positions and powers, it obtains a high resolution around the rearview mirror, and detects both strong ones on the front wheel and weak ones on the front cover.

Above all, two experiment results well agree with the simulations in Section 5. The proposed approach are proved to be able to achieve the super-resolutions, suppression of the background noise and wide dynamic range of power estimations of $10dB$.

6.3. Results of wide-band data

Based on the effectiveness and feasibility at single frequency, we show performance comparisons for the wide-band data of $[2400, 2600]Hz$, as Fig.10 illustrated. Each method obtains a better result than the correspondent one at $2500Hz$ in Fig.8. This is because that real sources are enforced and the flashing false alarms are suppressed over the wide-band average. The reconstruction of DAMAS in Fig.10a is acceptable, but its spatial resolution is not high enough on the front wheel and rearview mirror; Fig.10b shows that CLEAN greatly ameliorates the resolution, but it holds up unexpected points under the car body; the SC-DAMAS in Fig.10c has the advantages of the CLEAN, but it could not detect the weak sources around the back wheel; finally, our proposed method in Fig.10d enforces the sparse distribution, and reconstructs more accurate source positions and powers both for strong sources around the front wheel and weak ones on the mirror and back wheel.

7. Hybrid data

It seems that the above experiments with real data are not sufficient to show the advantages of our proposed methods. This is because the real sources generated by wind flow are not exactly known beforehand. To further verify our methods, we propose to use hybrid data by adding known synthetic sources to real data. In order to avoid overlapping real sources, synthetic sources are set on the region where there are no real sources as shown in Fig.11a.

7.1. The synthetic sources model

Based on the assumptions in Section 2.1, we suppose K' Gaussian white process $\mathbf{x}(t) = \{x_k(t),\, k = 1, \cdots, K'\}$, with $x_k(t) \sim \mathbb{N}(0, \sigma_k^2)$, and σ_k^2 is the variance of the kth variable. In order to generate wide-band sources $\{s_k(t),\, k = 1, \cdots, K\}$, $x_k(t)$ is convoluted by the impulse response $h(t)$ (for instance Blackman filter). Thus the synthetic sources are modeled by

$$s_k(t) = x_k(t) * h(t), \quad k = 1, \cdots, K', \tag{33}$$

where $*$ denotes convolution operation. Propagation delays are calculated using the forward model of Eq.(7), and synthetic data are summed to the real data.

7.2. Results on hybrid data

Five synthetic extended sources with different patterns are generated as seen in Fig.11a; their powers are within $[-4.5, 0]dB$. Fig.11 gives the results of various methods at $f = 2500Hz$. For the synthetic sources, Fig.11f shows that proposed approach successfully detects most of them with more precise estimations of positions and powers; meanwhile, for real sources in hybrid data, the proposed method better reconstructs both strong and weak sources on two wheels and rearview mirrors; moreover, it obtains a better noise suppression, comparing to the state of art methods: the conventional beamforming, DAMAS, DR-DAMAS, CLEAN and SC-DAMAS.

8. Conclusion

For near-field wide-band aeroacoustic imaging in poor SNR case, we propose a robust super-resolution approach

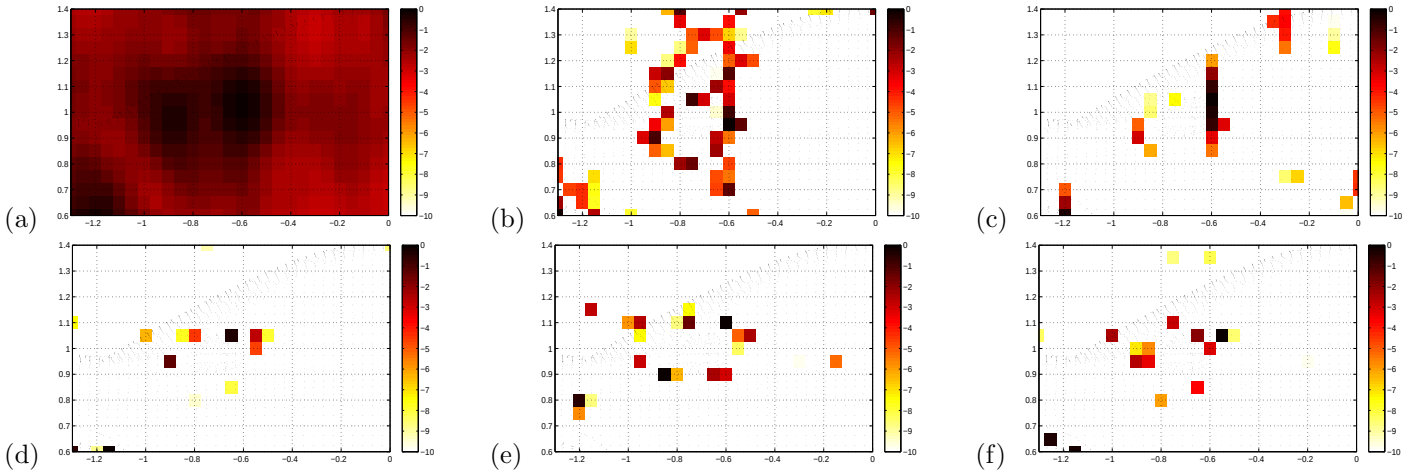

Figure 9: Acoustic imaging of rearview mirror at $2500Hz$: (a) Beamforming (b) DAMAS (5000i) (c) DR-DAMAS (5000i) (d) CMF (e) SC-DAMAS and (f) Proposed SC-RDAMAS

via sparsity constraint to estimate source powers and positions, and jointly estimate the variance of background noise and the parameter of sparsity constraint.

Simulations show that proposed method can obtain a super spatial resolution as high as $\Delta B = \arg\tan\frac{\Delta x_p}{D} \approx 0.6^\circ$ $(5cm)$ comparing to the one $(31cm)$ of the beamforming, and a $10dB$ dynamic range of power estimations; moreover it can detect both the monopole and extended sources with various patterns. Real data results demonstrate that proposed approach can successfully reconstruct strong sources on the front wheels and rearview mirrors, as well as weak sources on the back wheels and side windows. Hybrid data experiments furthermore proves the effectiveness of our methods that it not only well reconstructs the known synthetic sources, but also offers expected and acceptable estimations of real data. The proposed methods is compared with some of the state-of-the-art methods: the conventional beamforming, DAMAS, DR-DAMAS, SC-DAMAS, CMF and CLEAN. Finally our advantages are robustness to noise, wide dynamic range, super spatial resolutions, feasibility to be used. However, in propoesed approach, the adaptive estimation of sparsity constraint increases the computing cost, but computational burden still remains moderate among mentioned methods. Therefore, proposed approach can be applied for monopole and extended source imaging based on the 2D non-uniform microphone array in open wind tunnel tests.

For future works, we are investigating a hierarchy Bayesian inference approach via sparsity enforcing priors to reconstruct non-stationary correlated sources in colored background noise.

Acknowledgment

The authors are deeply grateful to Renault SAS, especially Mr. Jean-Luc Adam for offering real data and valuable discussions on our research.

References

[1] J. Lanslots, F. Deblauwe, K. Janssens, Selecting Sound Source Localization Techniques for Industrial Applications, Journal of Sound and Vibration 44 (6) (2010) 6–10.

[2] U. Michel, History of acoustic beamforming, in: Berlin Beamforming Conference 2006 (BeBeC2006), no. 1, Berlin, Germany, Feb.20-21,2006.

[3] H. V. Wal, P. Sijtsma, Source localization techniques with acoustic arrays at NLR, in: NAG/DAGA 2009 International Conference on Acoustics, NAG/DAGA, 2009.

[4] A. B. Nagy, Aeroacoustics research in Europe: The CEAS-ASC report on 2010 highlights, Journal of Sound and Vibration 330 (21) (2011) 4955–4980.

[5] M. Magalhaes, R. Tenenbaum, Sound sources reconstruction techniques: A review of their evolution and new trends, Acta Acustica united with Acustica 90 (2) (2004) 199–220.

(a)

(b)

(c)

(d)

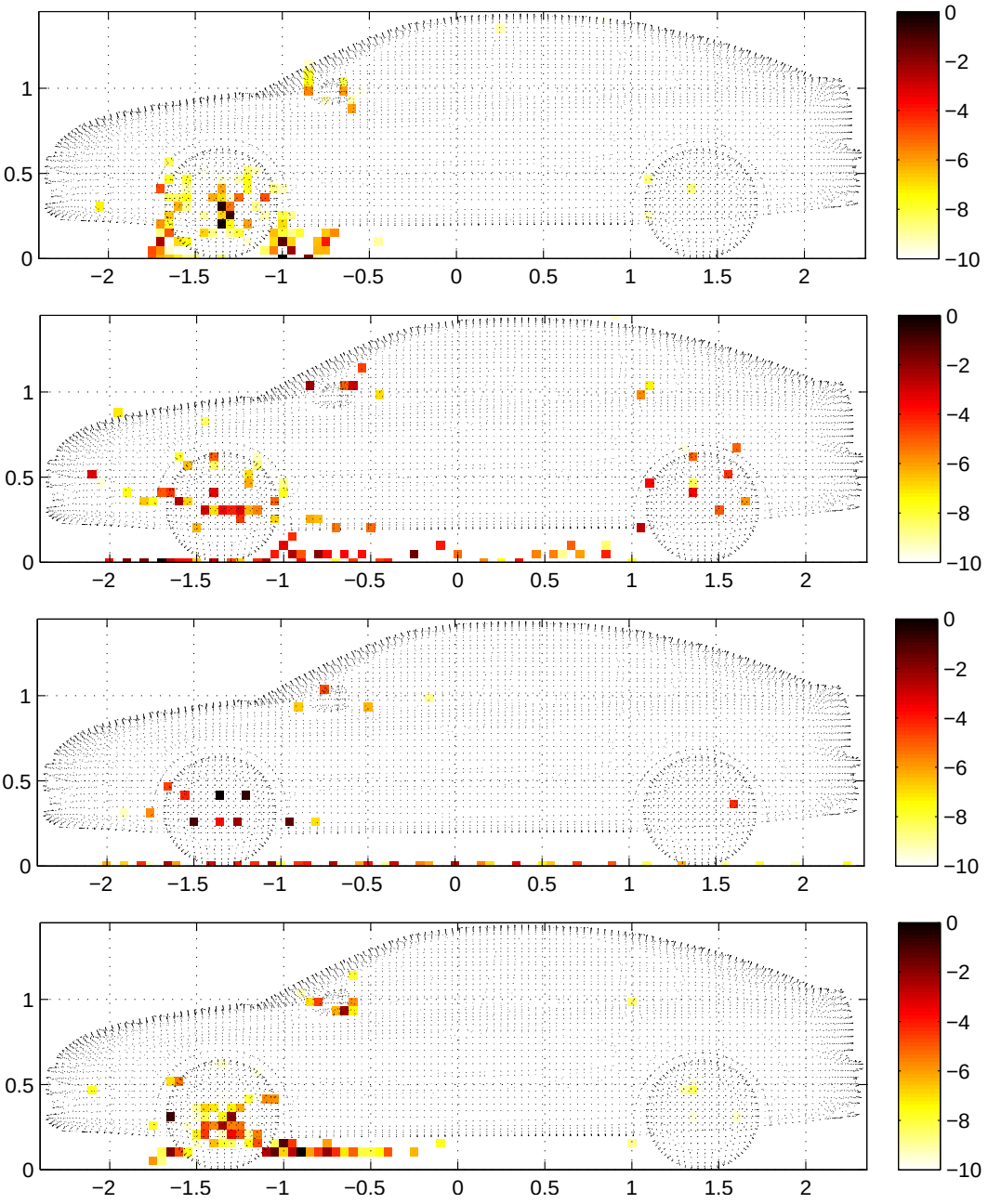

Figure 10: Wideband data over $[2400, 2600]Hz$: (a) DAMAS (b) CLEAN (c) SC-DAMAS and (b) Proposed SC-RDAMAS

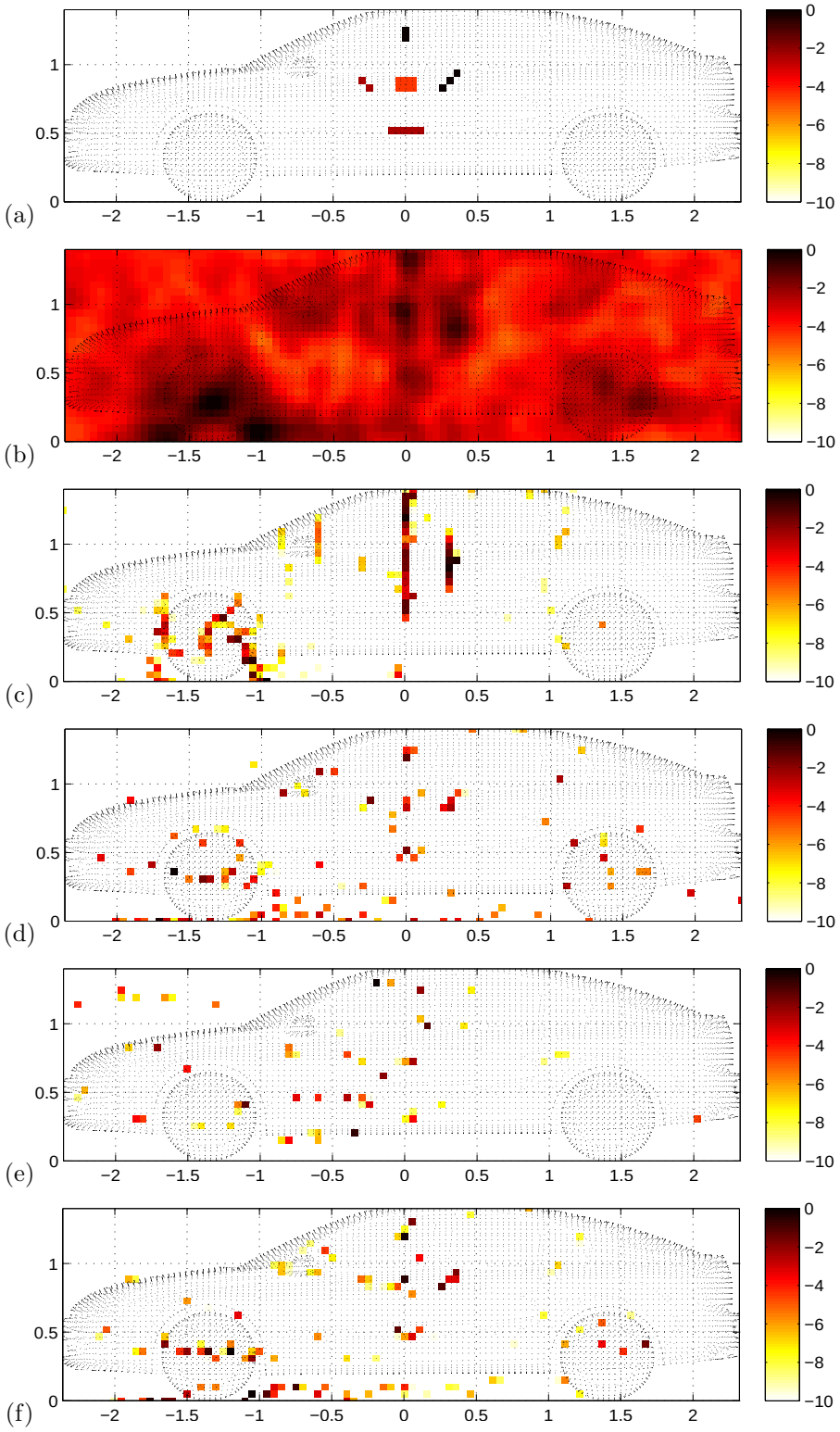

Figure 11: Acoustic imaging for hybrid data at $2500Hz$:(a) Simulated sources (b) Beamforming (c) DAMAS (5000i) (d) CLEAN (e) SC-DAMAS and (f) Proposed SC-RDAMAS.

[6] J. Chen, K. Yao, R. Hudson, Source localization and beamforming, Signal Processing Magazine, IEEE 19 (2) (2002) 30–39.

[7] A. Menoret, N. Gorilliot, J.-L. Adam, Acoustic imaging in wind tunnel S2A, in: 10th Acoustics conference (ACOUSTICS2010), Lyon, France, 2010.

[8] H. Siller, Localisation of sound sources on aircraft in flight, in: Berlin Beamforming Conference 2012, no. 1, Berlin, Germany, Feb.22-23,2012.

[9] L. Koop, S. Krber, T. Ahlefeldt, K. Ehrenfried, C. Spehr, Microphone-array measurements in wind tunnels: Challenges and limitations, in: Berlin Beamforming Conference 2012, no. 18, Berlin, Germany, Feb.22-23,2012.

[10] C. E. Kassis, J. Picheral, C. Mokbel, Advantages of nonuniform arrays using root-music, Signal Processing (2010) 689–695.

[11] J. D. Maynard, E. G. Williams, Y. Lee, Nearfield acoustic holography: I. Theory of generalized holography and the development of NAH 78 (4) (1985) 1395–1413.

[12] S. M. Dumbacher, D. L. Brown, J. R. Blough, R. W. Bono, Practical aspects of making NAH measurements, SAE transactions 108 (PART 2) (2000) 3081–3090.

[13] B. D. Van Veen, K. M. Buckley, Beamforming: A versatile approach to spatial filtering, IEEE ASSP Magazine 5 (1988) 4–24.

[14] R. O. Schmidt, Multiple emitter location and signal parameter estimation, IEEE Transactions on Antennas and Propagation 34 (1986) 276–280.

[15] E. Sarradj, A fast signal subspace approach for the determination of absolute levels from phased microphone array measurements, Journal of Sound and Vibration 329 (9) (2010) 1553–1569.

[16] M. D. Collins, W. A. Kuperman, Focalization: Environmental focusing and source localization, The Journal of the Acoustical Society of America 90 (3) (1991) 1410–1422.

[17] J. Antoni, Bayesian localisation: an approach unifies the inverse problem on acoustics, in: 10th Acoustics conference (ACOUSTICS2010), SFA, Lyon, 12-16 Avril 2010.

[18] P. Sijtsma, Clean based on spatial source coherence, International Journal of Aeroacoustics 6 (4) (2007) 357–374. doi:10.1260/147547207783359459.

[19] Y. Wang, J. Li, P. Stoica, M. Sheplak, T. Nishida, Wideband relax and wideband clean for aeroacoustic imaging, Journal of Acoustical Society of America 115 (2) (2004) 757–767.

[20] T. Brooks, W. Humphreys, A Deconvolution Approach for the Mapping of Acoustic Sources (DAMAS) determined from phased microphone arrays, Journal of Sound and Vibration 294 (4-5) (2006) 856–879. doi:DOI: 10.1016/j.jsv.2005.12.046.

[21] R. Dougherty, Extensions of DAMAS and Benefits and Limitations of Deconvolution in Beamforming, in: 11th AIAA/CEAS Aeroacoustics Conference, 2005, pp. 1–13.

[22] Q. Leclère, Acoustic imaging using under-determined inverse approaches: Frequency limitations and optimal regularization, Journal of Sound and Vibration 321 (3-5) (2009) 605–619.

[23] C. Lowis, P. Joseph, Determining the strength of rotating broadband sources in ducts by inverse methods, Journal of Sound and Vibration 295 (3-5) (2006) 614–632.

[24] T. Yardibi, J. Li, P. Stoica, L. Cattafesta III, Sparsity constrained deconvolution approaches for acoustic source mapping, The Journal of the Acoustical Society of America 123 (2008) 2631–2642.
URL http://dx.doi.org/10.1121/1.2896754

[25] T. Yardibi, J. Li, P. Stoica, N. S. Zawodny, L. N. Cattafesta, A covariance fitting approach for correlated acoustic source mapping, Journal of The Acoustical Society of America 127 (2010) 2920–2931.
URL http://dx.doi.org/10.1121/1.3365260

[26] D. Malioutov, M. Çetin, A. Willsky, A sparse signal reconstruction perspective for source localization with sensor arrays, Signal Processing, IEEE Transactions on 53 (8) (2005) 3010–3022.

[27] N. P. Galatsanos, A. K. Katsaggelos, Methords for choosing the regularization parameters and estimating the noise variance in image restoration and thier relation, IEEE Transactions on Image Processing 1 (3) (1992) 332–336.

[28] T. Suzuki, ℓ_1 generalized inverse beam-forming algorithm resolving coherent/incoherent, distributed and multipole sources, Journal of Sound and Vibration 330 (24) (2011) 5835 – 5851. doi:10.1016/j.jsv.2011.05.021.

[29] N. CHU, A. M. Djafari, J. Picheral, Robust bayesian super-resolution approach via sparsity enforcing priors for near-field wideband aeroacoustic source imaging, Journal of Sound and Vibration (vol.0, no.0) (2012) 0.

[30] A. Mohammad-Djafari, Bayesian approach with prior models which enforce sparsity in signal and image processing, EURASIP Journal on Advances in Signal Processing 2012 (1) (2012) 52. doi:10.1186/1687-6180-2012-52.
URL http://asp.eurasipjournals.com/content/2012/1/52

[31] T. Brooks, W. Humphreys Jr, Extension of DAMAS Phased Array Processing for Spatial Coherence Determination(DAMAS-C), in: 12th AIAA/CEAS Aeroacoustics Conference, American Institute of Aeronautics and Astronautics, 2006.

[32] T. Blumensath, M. Yaghoobi, M. Davies, Iterative hard thresholding and ℓ_0 regularisation, in: Acoustics, Speech and Signal Processing, 2007. ICASSP 2007. IEEE International Conference on, Vol. 3, IEEE, 2007, pp. 877–880.

[33] R. Tibshirani, Regression shrinkage and selection via the lasso, Journal of the Royal Statistical Society. Series B (Methodological) (1996) 267–288.

[34] S. Chen, D. Donoho, M. Saunders, Atomic decomposition by ba-

sis pursuit, SIAM journal on scientific computing 20 (1) (1999) 33–61.

[35] I. Daubechies, M. Defrise, C. De Mol, An iterative thresholding algorithm for linear inverse problems with a sparsity constraint, Communications on pure and applied mathematics 57 (11) (2004) 1413–1457.

[36] R. Chartrand, W. Yin, Iteratively reweighted algorithms for compressive sensing, in: Acoustics, Speech and Signal Processing, 2008. ICASSP 2008. IEEE International Conference on, IEEE, 2008, pp. 3869–3872.

[37] J. Fuchs, Multipath time-delay detection and estimation, Signal Processing, IEEE Transactions on 47 (1) (1999) 237–243.

[38] Y. Kim, P. Nelson, Optimal regularisation for acoustic source reconstruction by inverse methods, Journal of sound and vibration 275 (3-5) (2004) 463–487.

[39] A. Bruckstein, D. Donoho, M. Elad, From sparse solutions of systems of equations to sparse modeling of signals and images, SIAM review 51 (1) (2009) 34.

[40] D. Donoho, Compressed sensing, Information Theory, IEEE Transactions on 52 (4) (2006) 1289–1306.

[41] D. Blacodon, Spectral estimation method for noisy data using a noise reference, Applied Acoustics 72 (1) (2011) 11–21.

[42] D. Blacodon, Array Processing for Noisy Data: Application for Open and Closed Wind Tunnels, AIAA J. 49 (1) (2011) 55–66.

[43] J. Bulté, Improvement of acoustic measurements with an array of microphones in aerodynamic wind tunnels., 13th AIAA/CEAS Aeroacoustics Conference (28th AIAA Aeroacoustics Conference) 21-23 May 2007 Rome.

[44] L. Potter, E. Ertin, J. Parker, M. Cetin, Sparsity and compressed sensing in radar imaging, Proceedings of the IEEE 98 (6) (2010) 1006–1020.

[45] S. Sahnoun, E. Djermoune, C. Soussen, D. Brie, Sparse multidimensional modal analysis using a multigrid dictionary refinement, EURASIP Journal on Advances in Signal Processing 2012 (1) (2012) 60.

[46] A. Massa, G. Oliveri, Bayesian compressive sampling for pattern synthesis with maximally sparse non-uniform linear arrays, IEEE Transactions on Antennas and Propagation (vol.59, no.10) (Feb. 2011) 467–681.

[47] J. F. Sturm, Using sedumi 1.02, a matlab toolbox for optimization over symmetric cones (1998).